https://doi.org/10.15302/frontphys.2025.033202

Supplementary Information for: " Emulating Thouless pumping in the interacting Rice-Mele model using superconducting qutrits "

Ziyu Tao,[1,2,3,*] Wenhui Huang,[1,2,3,*] Jingjing Niu,[2,*] Libo Zhang,[1,2,3,*] Yongguan Ke,[4,5] Xiu Gu,[1,2,3] Ling Lin,[4] Jiawei Qiu,[1,2,3] Xuandong Sun,[1,2,3] Xiaohan Yang,[1,2,3] Jiajian Zhang,[1,2,3] Jiawei Zhang,[1,2,3] Yuxuan Zhou,[1,2,3] Xiaowei Deng,[1,2,3] Changkang Hu,[1,2,3] Ling Hu,[1,2,3] Jian Li,[1,2,3] Yang Liu,[1,2,3] Dian Tan,[1,2,3] Yuan Xu,[1,2,3] Tongxing Yan,[1,2,3] Yuanzhen Chen,[1,2,3,6,†] Chaohong Lee,[4,‡] Youpeng Zhong,[1,2,3,§] Song Liu,[1,2,3] and Dapeng Yu[1,2,3,6,¶]

[1] *Shenzhen Institute for Quantum Science and Engineering, Southern University of Science and Technology, Shenzhen 518055, China*
[2] *International Quantum Academy, Shenzhen 518048, China*
[3] *Guangdong Provincial Key Laboratory of Quantum Science and Engineering, Southern University of Science and Technology, Shenzhen 518055, China*
[4] *Institute of Quantum Precision Measurement, State Key Laboratory of Radio Frequency Heterogeneous Integration, College of Physics and Optoelectronic Engineering, Shenzhen University, Shenzhen 518060, China*
[5] *Laboratory of Quantum Engineering and Quantum Metrology, School of Physics and Astronomy, Sun Yat-Sen University (Zhuhai Campus), Zhuhai 519082, China*
[6] *Department of Physics, Southern University of Science and Technology, Shenzhen 518055, China*

(Dated: December 13, 2024)

Contents

* These authors contributed equally to this work.
† chenyz@sustech.edu.cn
‡ chleecn@szu.edu.cn
§ zhongyp@sustech.edu.cn
¶ yudp@sustech.edu.cn

I. Superconducting qutrit

A. Qutrit control

In superconducting circuits, a transmon qutrit [1–3] is realized by replacing the linear inductor of a quantum harmonic oscillator with a Josephson junction, which can be described by the Hamiltonian [2]

$$H = 4E_C n^2 - E_J \cos(\phi), \tag{1}$$

where n is the charge number operator, ϕ is the phase operator, obeying the commutation relation $[\phi, n] = i$, E_J is the Josephson energy, $E_C = e^2/(2C_\Sigma)$ is the charging energy, specified by the total capacitance C_Σ of the qutrit, and the transmon operating regime $E_J/E_C \gg 1$. By introducing the creation and annihilation operators $a, a^\dagger$

$$\begin{aligned} \phi &= \left(\frac{2E_C}{E_J}\right)^{1/4} \left(a^\dagger + a\right), \\ n &= \frac{i}{2}\left(\frac{E_J}{2E_C}\right)^{1/4} \left(a^\dagger - a\right), \end{aligned} \tag{2}$$

the system Hamiltonian can be approximated as a multilevel system [2]

$$H_q = \hbar\omega_{10} a^\dagger a - \frac{E_C}{2} a^\dagger a^\dagger a a = \sum_m E_m |m\rangle\langle m|, \tag{3}$$

where $E_1 - E_0 = \hbar\omega_{10}$, $E_2 - E_1 = \hbar\omega_{10} - E_C$. The subspace spanned by the three lowest-lying energy states $|0\rangle$, $|1\rangle$ and $|2\rangle$ forms an effective three-level system.

The frequency-tunable Xmon qutrit [4] used in our experiments is a variant of the transmon qutrit, where the single Josephson junction is replaced with two parallel junctions forming a superconducting quantum interference device (SQUID), and the Hamiltonian is given as [2]

$$H = 4E_C n^2 - E_{J1}\cos(\phi_1) - E_{J2}\cos(\phi_2), \tag{4}$$

where $E_{J1,J2}$ are the Josephson energy of the junction $1,2$ and $\phi_{1,2}$ are the phase difference across the junction $1,2$. By applying an external flux Φ, the SQUID loop has $\phi_1 - \phi_2 = 2\pi\Phi/\Phi_0 + 2\pi m$, where m is integer, $\Phi_0 = 2.067 \times 10^{-15}$ Wb is the flux quantum. The Hamiltonian in the presence of external flux can then be rewritten as [1]

$$H = 4E_C n^2 - E_J(\Phi)\cos(\phi - \phi_0), \tag{5}$$

which gives an effective flux-tunable Josephson energy

$$E_J(\Phi) = E_{J\Sigma} \cos\left(\frac{\pi\Phi}{\Phi_0}\right) \sqrt{1 + d^2 \tan^2\left(\frac{\pi\Phi}{\Phi_0}\right)}, \tag{6}$$

with $E_{J\Sigma} = E_{J1} + E_{J2}$, junction asymmetry $d = (E_{J2} - E_{J1})/(E_{J2} + E_{J1})$, $\tan\phi_0 = d\tan(\pi\Phi/\Phi_0)$, and the average phase difference $\phi = (\phi_1 + \phi_2)/2$. Therefore, the transmon frequency $\omega_{10} = \omega_{10}(\Phi)$ can be tuned by varying the external flux through the qutrit Z control [1].

The charge noise decreases exponentially with E_J/E_C in the transmon regime $E_J/E_C \gg 1$ [1]. For frequency-tunable qutrits, the transmon regime may be broken when varying E_J near the minimum point if the junction asymmetry $d = 0$. To keep under control the noise effect and anharmonicity of the qutrit, we use two asymmetric junctions designed as $d \approx 0.6$ and maintain the transmon regime $E_J(\Phi)/E_C \gg 1$ when varying the qutrit frequencies. In our system, the charging energy $E_C = e^2/(2C_\Sigma)$ is designed by specifying the total capacitance C_Σ of our qutrit chip, $E_C/h \approx 190$ MHz, the flux-tunable Josephson energy $E_J(\Phi)/h = 9.5 \sim 18.5$ GHz, thus the ratio $E_J(\Phi)/E_C = 50 \sim 97 \gg 1$ is kept in the transmon regime all the time.

B. Quantum simulation of the Rice-Mele model

Our 1D array of superconducting qutrits can be described by the Hamiltonian [5, 6]:

$$\begin{aligned} H/\hbar = &\sum_{j=1}^{N-1} \left(g_{j,j+1} a_j^\dagger a_{j+1} + \text{H.c.}\right) + \\ &\sum_{j=1}^{N} \left(\omega_j a_j^\dagger a_j - \frac{E_C}{2} a_j^\dagger a_j^\dagger a_j a_j\right). \end{aligned} \tag{7}$$

Moving to a frame rotating at the frequency ω, the effective Hamiltonian is given as:

$$\begin{aligned} H_{rot}/\hbar = &\sum_{j=1}^{N-1} \left(g_{j,j+1} a_j^\dagger a_{j+1} + \text{H.c.}\right) + \\ &\sum_{j=1}^{N} \left(\Delta_j a_j^\dagger a_j + \frac{U}{2} a_j^\dagger a_j^\dagger a_j a_j\right), \end{aligned} \tag{8}$$

where $\Delta_j = \omega_j - \omega$, $U = -E_C$. By configuring the qutrit frequencies and coupling strengths as

$$\begin{aligned} g_{j,j+1} &= -J + (-1)^j \delta, \\ \Delta_j &= (-1)^j \Delta, \end{aligned} \tag{9}$$

we can simulate the Hamiltonian of Rice-Mele model in the main text.

The state preparation of each superconducting qutrit is realized by applying a microwave pulse with frequency ω_d on the corresponding qutrit through its XY line. In the rotating frame of the driving frequency ω_d, the single-qutrit system can be described by the Hamiltonian [2]

$$H_d/\hbar = \Delta_d a^\dagger a + \frac{U}{2} a^\dagger a^\dagger a a + \frac{A_d}{2}\left(e^{i\phi_d} a + e^{-i\phi_d} a^\dagger\right), \tag{10}$$

where $\Delta_d = \omega_{10} - \omega_d$, A_d is the pulse amplitude, and ϕ_d is the pulse phase. Considering only the lowest three energy levels $|0\rangle, |1\rangle, |2\rangle$, the Hamiltonian is written in the matrix form as

$$H'_d/\hbar = \begin{pmatrix} 0 & A_d e^{i\phi_d}/2 & 0 \\ A_d e^{-i\phi_d}/2 & \Delta_d & \sqrt{2}A_d e^{i\phi_d}/2 \\ 0 & \sqrt{2}A_d e^{-i\phi_d}/2 & 2\Delta_d + U \end{pmatrix}. \tag{11}$$

When $\omega_{10} - \omega_d = \Delta_d = 0$, $A_d \ll \omega_{10}, |U|$, the microwave drive realizes a Rabi oscillation between $|0\rangle, |1\rangle$ [2]. The single-particle state $|1_j\rangle$ can be prepared from the ground state $|0\rangle$ by applying a so-called π pulse on the qutrit j, where $\int_0^{t_g} A_d(t)dt = \pi$, t_g is the pulse duration, and $\omega_d = \omega_{10}$.

C. State preparation for $|2\rangle$

To prepare the second excited state $|2\rangle$, we apply a microwave drive pulse on the qutrit j with the driving frequency $\omega_d = \omega_{20}/2 = \omega_{10} + U/2$, which is described by the Hamiltonian in the subspace of states $|0\rangle, |1\rangle, |2\rangle$:

$$H/\hbar = \frac{1}{2}\begin{pmatrix} 0 & A_d e^{i\phi_d} & 0 \\ A_d e^{-i\phi_d} & -U & \sqrt{2}A_d e^{i\phi_d} \\ 0 & \sqrt{2}A_d e^{-i\phi_d} & 0 \end{pmatrix}. \tag{12}$$

In the case of $A_d \ll U$, the system can be effectively reduced to a two-level system of $\{|0\rangle, |2\rangle\}$ [7]. The population oscillates between states $|0\rangle$ and $|2\rangle$ with the generalized Rabi frequency $\Omega_{20} = \sqrt{2}A_d^2/(4\pi|U|)$ [7], where

$$P_{|2\rangle} = \sin^2(\Omega_{20}t/2), \tag{13}$$

if the initial state is $|0\rangle$. In our experiment, we calibrate the two-photon excitation by scanning evolution time and driving frequency around $\omega_{20}/2$, as shown in Supplementary Fig. 1(a) and (b). The measured two-photon Rabi oscillations of $|0\rangle$ and $|2\rangle$ when $\omega_d = \omega_{20}/2$ is given in Supplementary Fig. 1(c). The initial two-particle Wannier state at the beginning of pumping process approximates to two particles at site j [8]. Supplementary Fig. 2(a) and (b) give examples of single- and two-particle Wannier state which approximates to $|1_j\rangle$ and $|2_j\rangle$ with large overlap.

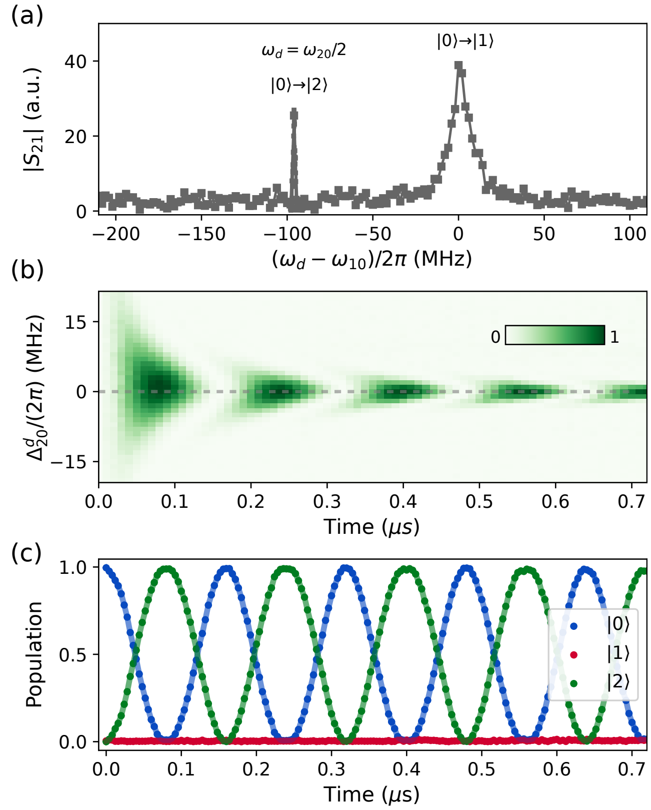

Supplementary Fig. 1. Experimental calibration for the two-photon excitation process. (a) Measured transmission S_{21} under the microwave driving with frequency ω_d, where the peak at $\omega_d = \omega_{20}/2$ indicates the state transition $|0\rangle \to |2\rangle$. (b) Measured population of state $|2\rangle$ with different frequency detuning $\Delta^d_{20} = \omega_d - \omega_{20}/2$ and evolution time. (c) Measured population of states $|0\rangle$, $|1\rangle$ and $|2\rangle$ under the microwave driving at frequency $\omega_d = \omega_{20}/2 = \omega_{10} + U/2$.

II. Coupling between superconducting qutrits

A. Control of tunable coupling

The coupling between the qutrits is realized by the T-shaped tunable couplers in our experiment, as shown in Fig. 1b of the main texts. The nearest-neighbour coupling strength can be controlled by applying external flux on the corresponding coupler [5]. The Hamiltonian of two qutrits QA, $Q_{\rm B}$ and a coupler C is given as [5]

$$\begin{aligned} H/\hbar = &\sum_{i=A,B,C}\left(\omega_i a_i^\dagger a_i + \frac{U_i}{2} a_i^\dagger a_i^\dagger a_i a_i\right) + \\ &g_{\rm AC}\left(a_A^\dagger a_C + a_A a_C^\dagger\right) + g_{\rm BC}\left(a_B^\dagger a_C + a_B a_C^\dagger\right) + \\ &g_{AB}\left(a_A^\dagger a_B + a_A a_B^\dagger\right), \end{aligned} \tag{14}$$

where ω_i is the qutrit or coupler frequencies, U_i is the qutrit or coupler anharmonicities, $g_{\rm AC}$ ($g_{\rm BC}$) is the coupling strength between $Q_{\rm A}$ ($Q_{\rm B}$) and coupler C, and g_{AB} is the coupling strength between $Q_{\rm A}$ and $Q_{\rm B}$. When $g_{\rm AC}, g_{\rm BC} \ll |\omega_{\rm A,B} - \omega_C|$, the effective Hamiltonian is given as [5]

$$\begin{aligned} H_{\rm eff}/\hbar = &\sum_{i=A,B}\left(\omega_i a_i^\dagger a_i + \frac{U_i}{2} a_i^\dagger a_i^\dagger a_i a_i\right) + \\ &g_{\rm eff}\left(a_A^\dagger a_B + a_A a_B^\dagger\right), \end{aligned} \tag{15}$$

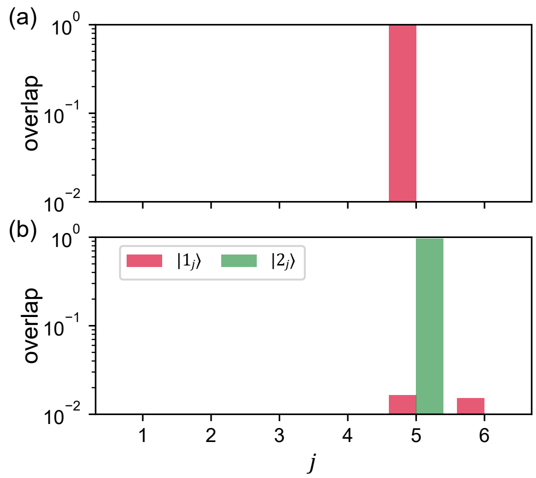

Supplementary Fig. 2. Example of numerically calculated (a) single-particle and (b) two-particle Wannier state ψ_w which approximates to first excited state $|1_j\rangle$ with overlap $|\langle\psi_w|1_j\rangle|^2$ larger than 0.99 and second excited state $|2_j\rangle$ with overlap $|\langle\psi_w|2_j\rangle|^2$ around 0.97, respectively. We consider (a) $\Delta_0/2\pi = 80$ MHz, $\delta_0/2\pi = J/2\pi = 8$ MHz, and (b) $\Delta_0/2\pi = 8$ MHz, $\delta_0/2\pi = J/2\pi = 12$ MHz at the evolution time $t = 0$.

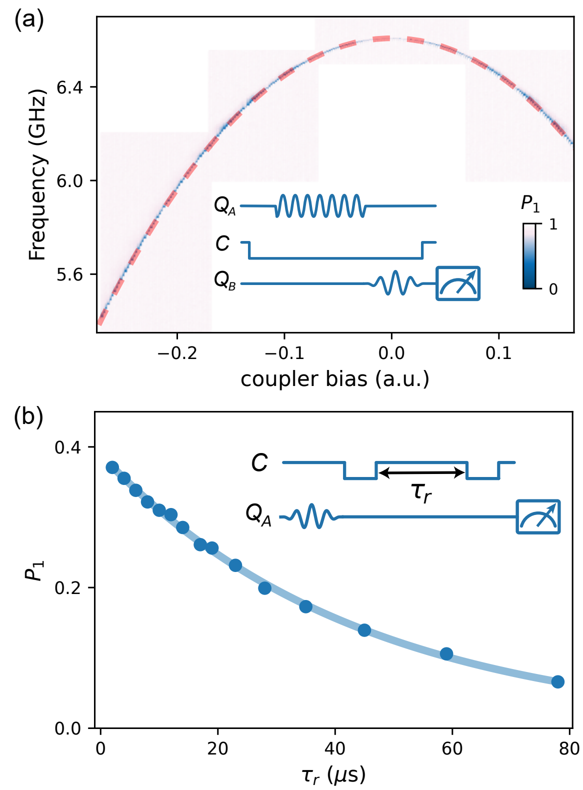

Supplementary Fig. 3. Characterization of the T-shaped transmon coupler. (a) Characterization of the coupler's frequency versus the coupler bias. (b) Lifetime T_1^c of the coupler, measured using the nearest neighboring qutrit $Q_{\rm A}$. The fitted coupler lifetime of $T_1^c = 43.9$ μs is consistent with the typical performance of transmon qutrits. Insets are control pulse sequences.

where the effective coupling strength

$$g_{\rm eff}(t) = g_{AB} + \frac{g_{\rm AC}g_{\rm BC}}{2}\left(\frac{1}{\omega_A - \omega_C(t)} + \frac{1}{\omega_B - \omega_C(t)}\right), \tag{16}$$

can be modulated by tuning the coupler frequency $\omega_C(t)$.

Directly measuring the coupler frequency $\omega_C(t)$ poses challenges due to the absence of a dedicated readout resonator and XY-control line for the coupler. Alternatively, we can indirectly probe the coupler's frequency through the nearest neighboring two qutrits utilizing the qutrit-coupler dispersive shift. This method involves applying a microwave pulse to the coupler through the XY control line of $Q_{\rm A}$, followed by monitoring the population of $Q_{\rm B}$. When the microwave resonates with the coupler frequency, $Q_{\rm B}$ experiences a small frequency shift. Subsequently, applying a Gaussian pulse to $Q_{\rm B}$ enables the detection of a decrease in its excited state population, facilitating the determination of the coupler's frequency via $Q_{\rm B}$. The relationship between the coupler's frequency and the amplitude of the coupler bias pulse is illustrated in Supplementary Fig. 3(a). In our experimental setup, the top coupler frequency is consistently designed at 6.5 GHz. The probed frequency closely aligns with the designed value. We note that the qutrit XY drive line incorporates a low-pass filter with a cutoff frequency of 5 GHz (see Fig. 7). Calibration of the coupler frequency is performed in a separate cooldown where the low-pass filter is removed.

At the top coupler frequency, we use the nearest neighboring qutrit to measure the lifetime T_1^c of the coupler. This is achieved by initially transferring a photon from the qutrit to the coupler, waiting for a duration τ_r, and subsequently extracting the photon. The population P_1 of the qutrit's excited state $|1\rangle$ is then measured, exhibiting exponential decay with a time constant T_1^c (Supplementary Fig. 3(b)). Fitting the experimental data yields $T_1^c = 43.9$ μs, a value comparable to the inherent coherence of transmon qutrits. Moreover, we perform vacuum Rabi oscillation between the first excited states of $Q_{\rm A}$ and $Q_{\rm B}$ at different coupler bias to characterize the effective coupling strength between qutrits. As shown in Supplementary Fig. 4, the coupling strength $g_{\rm eff}$ can be continuously adjusted from 3 MHz to approximately -25 MHz. We individually tune the coupler frequency to cancel the disorders and attain the desired coupling strength, calibrated by measuring the vacuum Rabi oscillation. The precision of calibration is limited by the maximum time scale before decoherence. Note that stronger coupling strength can be achieved by tuning the coupler frequency closer to the qutrit frequencies. However, this adjustment induces undesired longitudinal ZZ interaction and hybridize the coupler states with the qutrit states [5, 9].

The coupling strength $g_{\rm eff}$ is maintained within the strong coupling regime [2], where $g_{\rm eff}$ is strong enough with respect to the energy relaxation and dephasing rates, *i.e.*, $1/T_1, 1/T_2 \ll g_{\mathrm{eff}}$, yet remains comparatively weaker than the qutrit frequencies, *i.e.*, $g_{\mathrm{eff}} \ll \omega_{\mathrm{A,B}}$. In this domain, characterized by $1/T_1, 1/T_2 \ll g_{\mathrm{eff}} \ll \omega_{\mathrm{A,B}}$, the coupling strength g_{eff} should be sufficiently strong to preserve coherence against environmental perturbations while being suitably limited with respect to the upper bound of $\omega_{\mathrm{A,B}}$ to conserve particle number, thus facilitating coherent transport in both single-particle and multi-particle scenarios. Moreover, for the strong interaction regime, g_{eff} should remain sufficiently small compared to the upper bound of $|U|$ [8], as necessitated by the strong interaction regime ($|U| \gg g_{\mathrm{eff}}$) for the transport of two-particle state.

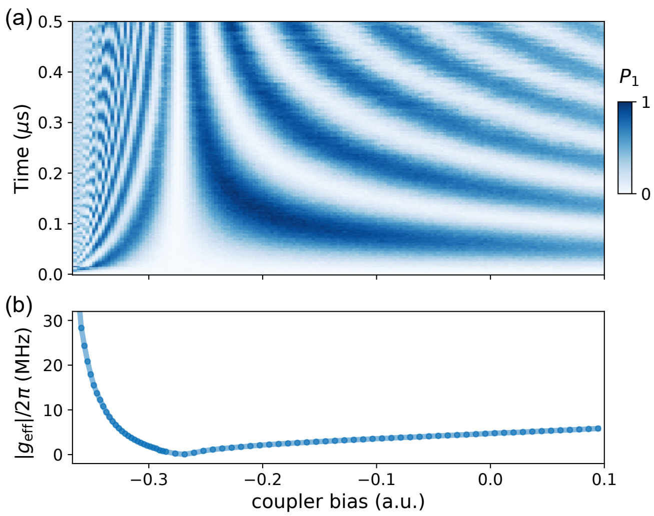

Supplementary Fig. 4. Characterization of tunable coupling. (a) Vacuum Rabi oscillation between Q_{A} and Q_{B} at different coupler bias, in which the colors denote the population P_1 of Q_{B}. (b) The tunable coupling strength g_{eff} extracted from the data of (a).

Instead of simply regarding the tunable couplers as tools of modulating hopping strengths, we could also take the couplers into full account and treat them as transmon qutrits, albeit lacking dedicated readout resonators for quantum state measurement. This full model enables us to incorporate the photon leakage into the couplers. The parameter modulation is the same as the single-particle pumping process in the main text: the modulated frequency $\Delta_0/2\pi = 80$ MHz, the effective modulated coupling strength $\delta_0/2\pi = J/2\pi = 8$ MHz, and the period $T = 0.4$ μs. Supplementary Fig. 5 gives the numerical results of pumping involving six qutrits and five couplers, with an initial microwave photon prepared in the third qutrit. During the pumping process, photon leakage into each coupler reaches as high as 0.1 during the pumping process, subsequently diminishing to 10^{-3} after each pumping period.

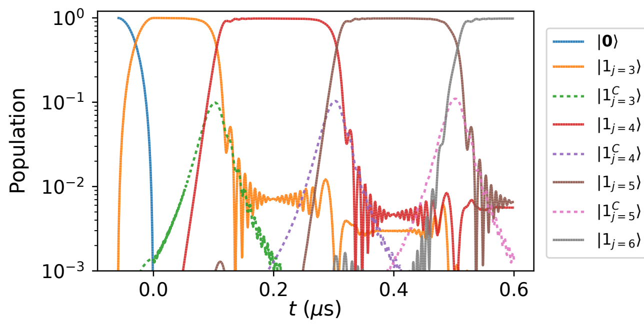

Supplementary Fig. 5. Numerical simulation treating couplers as qutrits. The first excited states of coupler C_j are given as $|1^C_j\rangle$. The initial state $|1_{j=3}\rangle$ is prepared by applying a π pulse of Q_3 on the ground state $|\mathbf{0}\rangle \equiv |00\cdots0\rangle$, which is given in the range of $t < 0$.

B. Tunable coupling of second-excited states

When focusing on the physics of the two particle states and restricting the Hilbert space to the subspace spanned by $|0\rangle$ and $|2\rangle$, due to weak nonlinearity, the original Hamiltonian (Eq. (15)) can induce an effective coupling Hamiltonian between the states $|0\rangle$ and $|2\rangle$, denoted as [8]

$$H^{|2\rangle}_{\mathrm{eff}}/\hbar = g^{|2\rangle}_{\mathrm{eff}} \left(b^\dagger_A b_B + b_A b^\dagger_B \right) + 2\Delta(-b^\dagger_A b_A + b^\dagger_B b_B), \tag{17}$$

where $b^\dagger_j|0\rangle = |2_j\rangle$ for $j = A, B$, and the qutrit frequency detuning $\omega_B - \omega_A = 2\Delta$. Treating the coupling term as the dominant term and the other as the perturbation term, the effective coupling strength follows the relation $g^{|2\rangle}_{\mathrm{eff}} = 2g^2_{\mathrm{eff}}/U$ [8]. Despite being an order of magnitude smaller than U due to $|g_{\mathrm{eff}}| \ll |U|$, it remains within the strong coupling regime. It is crucial to note that this coupling strength relation deviates from the theoretical formula in the presence of a coupler. To illustrate the two-body physics entailed in the coupling of our system, we characterize the coupling relation through the transport of the second excited state $|2\rangle$. Using a similar approach to the calibration of the effective coupling strength for the first excited state g_{eff}, we extract the effective coupling strength $g^{|2\rangle}_{\mathrm{eff}}$ of the second excited state $|2\rangle$ by observing the oscillation between $|2_A\rangle$ and $|2_B\rangle$. As shown in Supplementary Fig. 6, the coupling strengths conform to the relation $g^{|2\rangle}_{\mathrm{eff}} = 2g^2_{\mathrm{eff}}/U$ when g_{eff} is small [8], and deviate for a large g_{eff} due to the frequency shift of the two particles state $|1_A\rangle|1_B\rangle$ induced by the coupler's longitudinal ZZ interaction [5, 9]. Despite additional corrections to the effective couplings in the pure two-qutrit case, the coherent transport and coupling strength of such two-body physics remain under control. This capability enables us to calibrate and control the many-body Hamiltonian in multi-qutrit experiments.

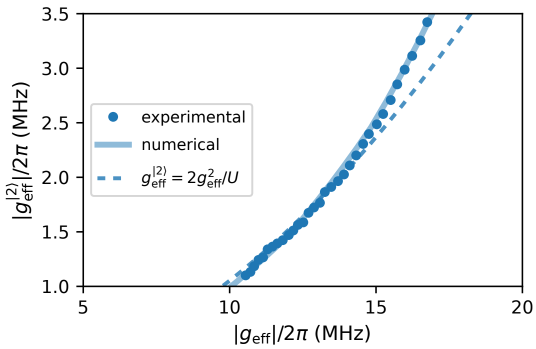

Supplementary Fig. 6. Characterization of the effective coupling strength of second excited state $g_{\rm eff}^{|2\rangle}$ at different $g_{\rm eff}$. The dashed line indicates the relation $g_{\rm eff}^{|2\rangle} = 2g_{\rm eff}^2/U$. The blue dots are experimental data, and the blue curve is numerical simulation of master equation including the qutrits and coupler.

III. Experimental setup

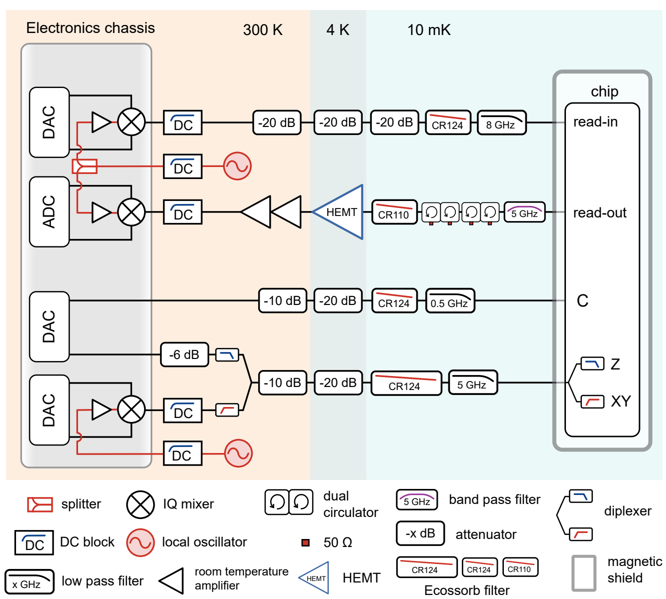

Supplementary Fig. 7. Room temperature and cryogenic wiring.

Supplementary Fig. 7 shows the room temperature and cryogenic wiring layout. We use custom made digital-to-analog converter (DAC) and analog-to-digital converter (ADC) circuit boards for qutrit control and measurement, respectively. The control boards have dual-channel 14-bit vertical resolution DAC integrated circuits operating at 1 Gs/s driven by a field-programmable gate array (FPGA) chip. Each DAC analog output is filtered by a custom Gaussian low-pass filter with 250 MHz bandwidth to filter the clock feedthrough, where the Gaussian spectrum of the filter ensures smooth impulse response in time domain. The DAC boards can generate nanosecond-length pulses for fast qutrit Z or coupler C control, or the two channels can modulate the in-phase and quadrature components of an IQ mixer for frequency up-conversion, providing several GHz frequency signals for qutrit XY control and dispersive readout. At room temperature, the XY and Z control signals of each qutrit are combined together with a diplexer and delivered to the device using one coaxial cable channel. The combined control signals are then split using an on-chip diplexer [10], in which the XY signal is capacitively coupled to the qutrit via an open-ended quarter-wavelength impedance matching line, while the Z signal is inductively coupled to the qutrit through another short-ended quarter-wavelength impedance matching line.

The ADC boards have dual-channel 8-bit vertical resolution ADC integrated circuits operating at 1 Gs/s driven by a FPGA chip. The qutrit dispersive readout output is first amplified by the cryogenic high electron mobility transistor (HEMT) manufactured by Low Noise Factory at the 4 K stage and two room-temperature low noise amplifiers, then downconverted with an IQ mixer, and finally digitized and demodulated by the ADC boards. Two cryogenic circulators are inserted between the device and the cryogenic HEMT to isolate reflections as well as thermal noise emitted from the input of the cryogenic HEMT to the device. The Eccorsorb CR110 and 5 GHz bandpass filters with low insertion loss at output signal frequency are used to block noise outside the bandwidth of circulators. Each control line is heavily attenuated and filtered at each temperature stage in the dilution refrigerator to minimize the impact on the qutrit coherence while retaining controllability.

The custom DAC/ADC boards receive power, communication, and clock synchronization through a custom backplane housed in a 5U chassis, which can host 21 DAC/ADC boards, see Supplementary Fig. 8(a). In our experiments, we used up to 84 boards, including 42 DAC boards for XY control, 36 DAC boards for Z control, and 6 ADC boards for data acquisition, all hosted in five chassis as illustrated in Supplementary Fig. 8(b). The chassis are synchronized with a 10 MHz reference clock, and the output signals of all boards are synchronized by trigger signals generated by a master board and distributed to other boards in the same chassis through the backplane, and distributed to other four chassis through coaxial cable connections. Communication between the host computer and the chassis is through a local area ethernet network. The electronics connection topology is depicted in Supplementary Fig. 8(c).

IV. Device Information

A. Device fabrication

The superconducting quantum processor used in this experiment is fabricated with the following steps:

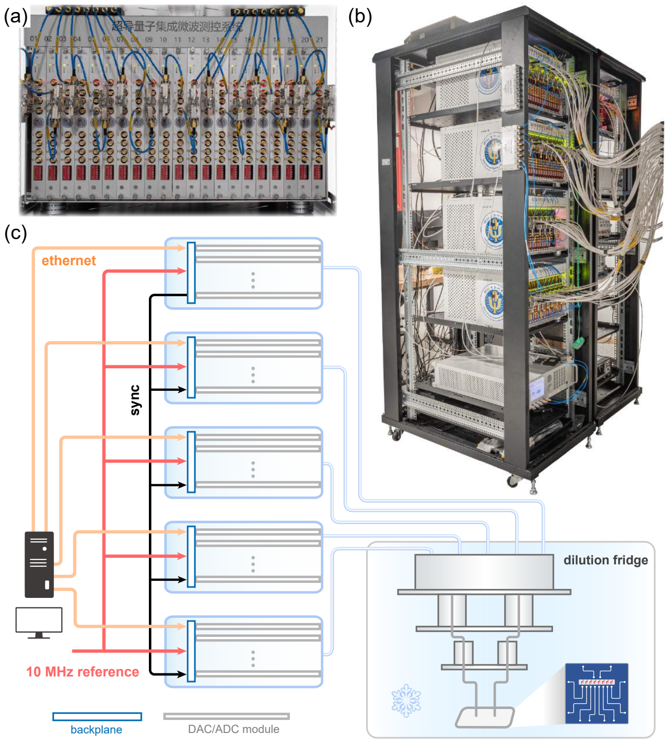

Supplementary Fig. 8. Microwave electronics for qutrit control and readout. (a) Photograph of a 5U chassis of custom made DAC/ADC modules. (b) Photograph of the microwave electronics setup housed in two 42U racks, consisting of 5 chassis of custom made DAC/ADC modules, together with microwave signal generators, splitters and diplexers etc. (c) Schematic of the electronics connection, showing the 10 MHz reference clock, the synchronization and the ethernet network topology.

1. A 100 nm aluminum film is deposited on a 4 inch c-plane sapphire wafer in Plassys MEB 550SL3.
2. Photo-lithography using laser direct writing, followed by inductively coupled plasma (ICP) dry etching to define the capacitor pads, readout resonators, control and readout circuits etc.
3. Photo-lithography using laser direct writing, followed by electron beam evaporation of 200 nm SiO_2 and lift-off to fabricate the scaffold layer for air-bridge crossovers.
4. Electron-beam lithography, followed by double-angle evaporations of aluminum in Plassys MEB 550SL3 and lift-off to fabricate the $Al/Al_2O_3/Al$ Josephson junctions.
5. Photo-lithography using laser direct writing, followed by electron beam evaporation of 300 nm aluminum and lift-off to fabricate the conducting layer for air-bridge crossovers and bandage for the Josephson junctions [11, 12], with *in situ* ion milling to create galvanic contact with the bottom aluminum layer fabricated in step 1.
6. Dice the wafer into individual dies.
7. Release the SiO_2 scaffold layer using vapor HF etch.

B. Device performance

In this experiment, we use asymmetric Josephson junctions with $\alpha = E_{J1}/E_{J2} = 3.3$ (4.3) on the odd (even) indexed qutrits, where E_{J1} and E_{J2} are the Josephson energies of the two qutrit junctions. With this configuration, the odd (even) indexed qutrits have a maximum frequency sweet spot near 4.9 GHz (5.1 GHz) and a minimum frequency sweet spot near 3.6 GHz (4.1 GHz), see Figure 9. The staggered frequency arrangement of the qutrits in the chain enables appropriate idling frequencies for optimal performance. The upper sweet point of qutrits is close to the readout resonators frequency range of 5–5.3 GHz, allowing for fast reset proposals [13]. The 36 readout resonators are divided into six groups, each group is coupled to a Purcell filter [14]. The Purcell filter functions as a bandpass filter, impeding microwave propagation at the qutrit frequency, and suppressing the Purcell decay rate. Limited by the qutrit frequency tuning range of approximately 4.1 GHz to 4.9 GHz, the staggered on-site energy $\Delta/2\pi$ can be adjusted from 0 to approximately 400 MHz. Additionally, the readout resonator frequencies (around 5.1 GHz) closely approach the upper bound of the qutrit frequencies. Consequently, the upper bound of $\Delta/2\pi$ is further constrained by Purcell decay when the qutrit frequencies approach that of the readout resonators. In this experiment, a maximum $\Delta/2\pi = 150$ MHz is employed, ensuring that the qutrits are detuned from their readout resonators by more than 500 MHz, thereby safely circumventing the impact of Purcell decay.

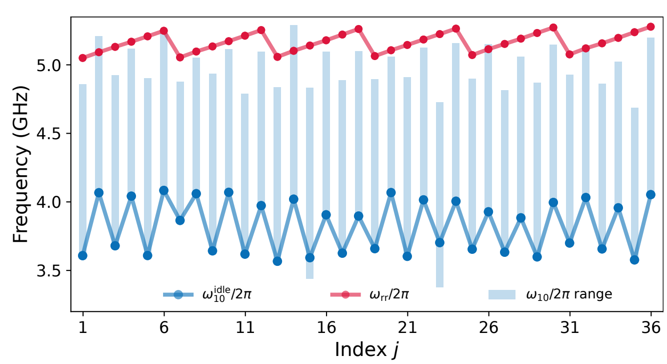

Supplementary Fig. 9. Characterization of qutrit frequencies $\omega_{10}/2\pi$ and readout resonator frequencies $\omega_{rr}/2\pi$. The blue lines denote the tuning range of qutrit frequencies, the blue dots denote the qutrit idling frequencies, and the red lines with dots denote the readout resonator frequencies.

The readout of the qutrit state involves probing the resonator's state-dependent frequency shift (dispersive shift), which is coupled but largely detuned from the qutrit. However, due to the resonator's spontaneous decay to the readout feed line, the qutrit experiences additional damping through the Purcell effect. To mitigate this effect, the above-mentioned Purcell filter can be used as a bandpass filter to impede microwave propagation at the qutrit frequency and suppress the Purcell decay rate. The center frequency of the Purcell filter used in our experiment is 5.15 GHz, with weak coupling to the input port and strong coupling to the output port, as seen in its transmission spectrum in Supplementary Fig. 10(a). By using this Purcell filter, high-quality, single-shot qutrit dispersive readout for states $|0\rangle, |1\rangle$ and $|2\rangle$ can be achieved, as demonstrated in Supplementary Fig. 10(b).

Supplementary Fig. 11 displays the qutrit readout fidelities, with an average state fidelity of 0.95 for the $|0\rangle$ state, 0.85 for the $|1\rangle$ state, and 0.81 for the $|2\rangle$ state, respectively.

Supplementary Fig. 12 illustrates the energy relaxation (T_1) and dephasing time (T_2) of each qutrit at its idling frequency.

C. Device control calibration

We consider the distorted Z pulse X_{qu} in the frequency domain that arrives at the qutrits as

$$X_{\mathrm{qu}}(\omega) = H(\omega) X_{\mathrm{in}}(\omega), \tag{18}$$

where $X_{\mathrm{in}}(\omega)$ is the input signal, and $H(\omega)$ is the transfer function. To correct this distortion, we perform a predistortion on our desired pulse $X(\omega)$ with the inverse of $H(\omega)$

$$X_{\mathrm{corr}}(\omega) = H^{-1}(\omega) X(\omega), \tag{19}$$

where

$$H(\omega) = 1 + \sum_{j=1}^{k} \frac{i a_j \omega}{i\omega + b_j} \tag{20}$$

describes multiple exponentially decaying overshoots ($a_j > 0$) or undershoots ($a_j < 0$) with decay rate b_j. One can identify such distortion by preparing a superposition state $|+\rangle = (|0\rangle + |1\rangle)/\sqrt{2}$ after applying the Z pulse, and subsequently monitoring the phase of the second $R_{\pi/2}(\phi)$ pulse. Figure 13 gives the phase ϕ as a function of the delay time t_{delay} before and after the correction of Z pulse.

The qutrits frequencies can be individually adjusted by Z control lines, where a typical relationship between the qutrit frequency and the bias is given in Supplementary Fig. 14.

V. Theoretical model and numerical simulation

A. Adiabatic shifting of a particle on a dimer

To understand the charge pumping protocol from the bottom up, we consider the simplest case with a single dimer only, i.e., two qutrits Q_1 and Q_2 tunably coupled to each other. The Hamiltonian reads

$$H_2(t)/\hbar = \Delta(t)(a_1^\dagger a_1 - a_2^\dagger a_2) + J(t)(a_1^\dagger a_2 + a_1 a_2^\dagger) \tag{21}$$

In the single excitation manifold, this Hamiltonian can be reduced to a spin Hamiltonian $\widetilde{H_2}/\hbar = \Delta(t)\sigma_z + J(t)\sigma_x$, where $\sigma_z = |10\rangle\langle 10| - |01\rangle\langle 01|$, and $\sigma_x = |10\rangle\langle 01| + |01\rangle\langle 10|$. We initialize the system with a particle at site 1 and then vary the qutrit frequencies and hopping strength as $\Delta = \Delta_0 \cos(\omega t)$, $J = J_0 \sin(\omega t)$. This is equivalent to a spin under a slowly rotating magnetic field. According to the adiabatic theorem, if H_2 is varied slowly enough, the particle will be shifted from $|10\rangle$ to $|01\rangle$ until $\omega t = \pi$.

B. Noninteracting Rice-Mele model

The second-quantization Hamiltonian of the system reads

$$H = \sum_{j,k} c_j^\dagger H_{j,k} c_k \tag{22}$$

where c_j is the creation operator of a particle at site j ($j = 1, 2, \cdots, N$) and H is the $N \times N$ matrix of hopping amplitudes in the Wannier basis. For noninteracting Rice-Mele model in the tight binding limit (Eq. 2 in the main text), the matrix $H/\hbar$ takes the form

$$\begin{pmatrix} \Delta & -J-\delta & 0 & \cdots & 0 & 0 \\ -J-\delta & -\Delta & -J+\delta & \cdots & 0 & 0 \\ 0 & -J+\delta & \Delta & \cdots & 0 & 0 \\ \cdots & \cdots & \cdots & \cdots & \cdots & \cdots \\ 0 & 0 & 0 & \cdots & \Delta & -J-\delta \\ 0 & 0 & 0 & \cdots & -J-\delta & -\Delta \end{pmatrix}. \tag{23}$$

In the thermodynamic limit ($N \to \infty$), the Rice-Mele Hamiltonian shows two energy bands separated by a gap with width $2\hbar\sqrt{\delta^2 + \Delta^2}$, which vanishes at the degeneracy point $\Delta = \delta = 0$.

C. Interacting Rice-Mele model

We consider the pumping process of N interacting particles in a periodically modulated lattice with spatial period d. The inter-particle interaction breaks the translation symmetry of individual particles. However, all the particles shifted as a whole to a unit cell to preserve the energy of the system. Therefore, the system has co-

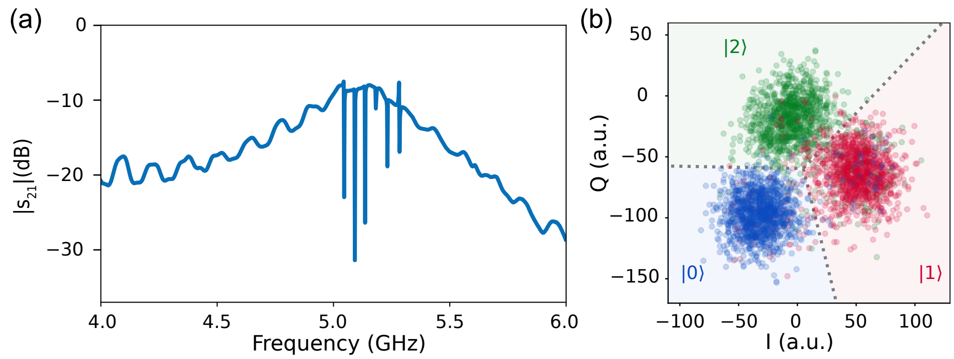

Supplementary Fig. 10. Single-shot qutrit dispersive readout with Purcell filter. (a) Measured transmission spectrum of the Purcell filter. (b) Single-shot dispersive readout for states $|0\rangle, |1\rangle, |2\rangle$ in the quadrature (IQ) space.

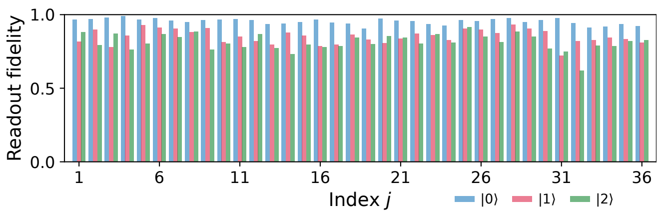

Supplementary Fig. 11. Characterization of readout fidelities for states $|0\rangle$, $|1\rangle$ and $|2\rangle$.

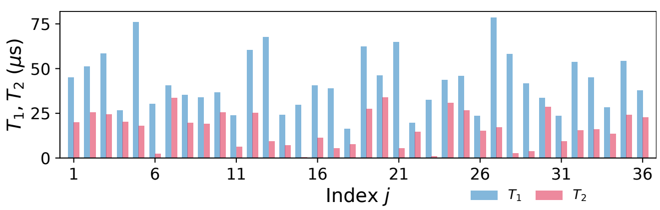

Supplementary Fig. 12. Characterization of energy relaxation time T_1 and dephasing time T_2.

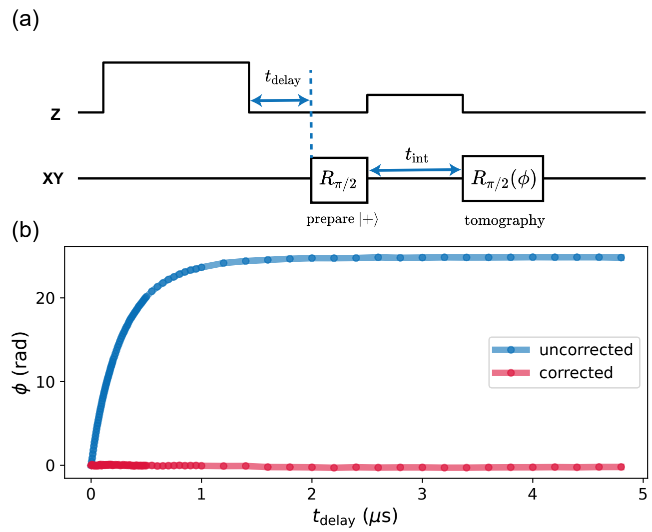

Supplementary Fig. 13. Correction of Z pulse distortion. (a) The pulse sequence used to measure Z pulse distortion. The first $R_{\pi/2}$ pulse is applied after the Z pulse with a delay time $t_{\rm delay}$ to prepare $|+\rangle = (|0\rangle + |1\rangle)/\sqrt{2}$, then the second $R_{\pi/2}(\phi)$ pulse for tomography is applied to obtain the accumulated phase during the integration time $t_{\rm int} = 100$ ns, where qutrit frequency is placed on a phase sensitive point during $t_{\rm int}$. (b) The accumulated phase as a function of $t_{\rm delay}$, where the blue and red curve are for the phases before and after the correction of pulse distortion, respectively.

translation symmetry, and the center-of-mass momentum K is a good quantum number [8]. With the co-translation symmetry, we can apply the multiparticle Bloch theorem to obtain the center-of-mass energy band $E_{m,K}$ and the associated multiparticle Bloch states $|\Psi_{m,K}\rangle$, where m is the band index. This is a multiparticle generalization of the conventional single-particle energy band.

If an initial state uniformly occupies the mth center-of-mass energy band, the mean position of particles is shifted by multiple unit cells in one pumping cycle T,

$$\langle \delta x \rangle = \langle x(T) \rangle - \langle x(0) \rangle = C_m d. \tag{24}$$

Here, C_m is the Chern number of the mth center-of-mass energy band, which is defined as

$$C_m = \frac{i}{2\pi} \int_0^{2\pi/d} dK \int_0^T dt (\langle \partial_t \Psi_{m,K} | \partial_K \Psi_{m,K} \rangle - \langle \partial_K \Psi_{m,K} | \partial_t \Psi_{m,K} \rangle). \tag{25}$$

Without loss of generality, we consider the Thouless pumping via the interacting Rice-Mele model described in the main text. Depending on the ratio between the interaction U and the potential well bias 2Δ of the neighboring lattices, there are two major different pumping phenomena in the two-body limit. When $|U| \gg |2\Delta|$ and $|U| \gg J, \delta$, two particles at the same site can be effectively viewed as a composite particle. In one pumping cycle, the two particles will be shifted by a unit cell as a whole. When $|U|$ is comparable to $|2\Delta|$ and $|U| \gg J, \delta$, there is negligible energy offset between bounded particles at the same site and two particles at

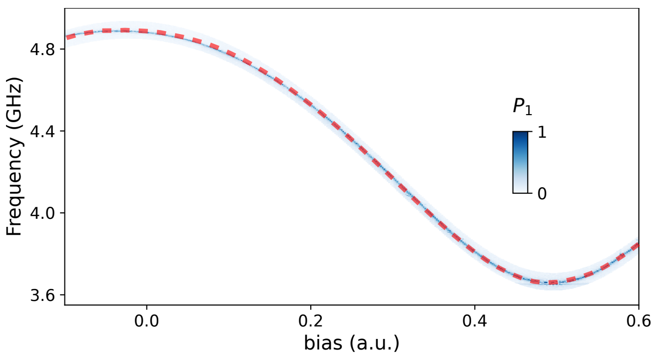

Supplementary Fig. 14. Characterization of the qutrit frequency $\omega_{10}/2\pi$ by spectroscopy. The colors denote the population P_1 of the qutrit, and the dashed line indicates the fitted frequency as a function of qutrit bias.

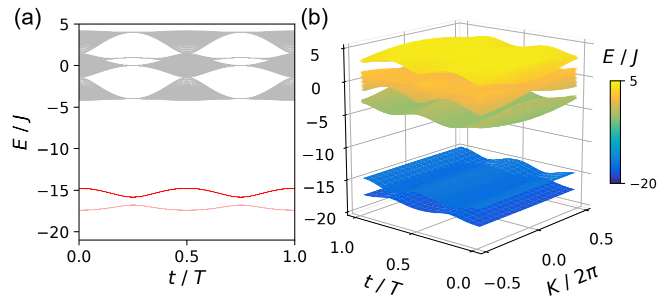

Supplementary Fig. 15. Center-of-mass energy band for Thouless pumping of bounded particles. (a) Energy spectrum as a function of time. (b) Center-of-mass energy band as functions of time and center-of-mass momentum. Here, the two-particle bound-state pumping is performed with the parameters of $\Delta_0/2\pi = 8$ MHz, $\delta_0/2\pi = J/2\pi = 12$ MHz and a pumping period of $T = 0.4$ μs.

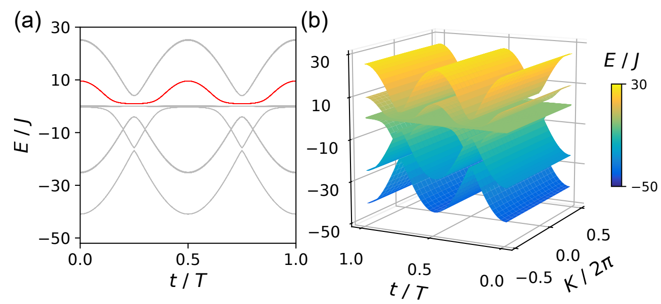

Supplementary Fig. 16. Center-of-mass energy band for resonant tunnelings. (a) Energy spectrum as a function of time. (b) Center-of-mass energy band as functions of time and center-of-mass momentum. The parameters are set as $\Delta_0/2\pi = 150$ MHz, $\delta_0/2\pi = J/2\pi = 12$ MHz and a pumping period of $T = 0.4$ μs.

nearest-neighboring sites, and resonant coupling between the two states can occur. In one pumping cycle, the resonant tunnelings happen four times and the two particles will be shifted one by one to a unit cell. In the following, we give a detailed theoretical analysis of Thouless pumping of bounded particles and resonant tunnelings.

D. Energy band for Thouless pumping of bounded particles

We calculate the center-of-mass energy band for the case of Thouless pumping of bounded particles; see Supplementary Fig. 15. The red and pink lines in Supplementary Fig. 15(a) indicate the energy bands for the bounded particles in which two particles are almost at the same site, while the grey lines indicate the energy bands for the scattering states in which two particles are almost independent. In the (K, t) space (Supplementary Fig. 15(b)), the Chern numbers of the center-of-mass energy bands for bounded particles are ± 1. If we prepare the initial state as two particles at the same odd (even) site, the initial state almost uniformly occupies the pink (red) energy spectrum. The two particles as a whole will be moved forward (backward) by a unit cell, corresponding to the Chern number $+1$ (-1). The experimental result on emulating Thouless pumping of bounded particles in the main text (Fig. 2) is consistent with this theoretical expectation.

E. Energy band for resonant tunnelings

The center-of-mass energy band for the case of resonant tunnelings is also calculated, as shown in Supplementary Fig. 16. Compared with the case for Thouless pumping of bounded particles, the energy spectrum becomes more complex. When the energy is around 0, there is an isolated energy band (red lines in Supplementary Fig. 16) that can explain resonant tunnelings. Around the energy-avoided crossing, the states $|2_j\rangle|0_{j+1}\rangle$ and $|1_j\rangle|1_{j+1}\rangle$ are strongly coupled, leading to the resonant tunneling between them. There are four energy-avoided crossing points, indicating that resonant tunnelings occur four times. In Supplementary Fig. 16(b), the Chern number of the isolated band for resonant tunnelings is $+1$. If we prepare the initial state as two particles at the same site, such an initial state almost uniformly occupies the isolated band around 0, the subsequent four resonant tunnelings give rise to quantized forward shift of two particles one by the other.

If we start from the initial Hamiltonian with no energy bias between adjacent sites, the initial state of two particles $|1_j\rangle|1_{j+1}\rangle$ can be expanded as a superposition of two symmetric and asymmetric states,

$$\begin{aligned}|1_j\rangle|1_{j+1}\rangle = &\frac{1}{2\sqrt{2}}\left[(|1_j\rangle + |1_{j+1}\rangle)\otimes(|1_j\rangle + |1_{j+1}\rangle)\right. \\ &\left.-(|1_j\rangle - |1_{j+1}\rangle)\otimes(|1_j\rangle - |1_{j+1}\rangle)\right].\end{aligned} \tag{26}$$

Without inter-particle interaction, the symmetric and asymmetric states uniformly occupy the single-particle lower and upper bands, which have opposite Chern numbers ±1, respectively. The symmetric and asymmetric states are respectively shifted forward and backward by one unit cell, and the center-of-mass positions cancel with each other, with no shift over a pumping cycle.

F. Edge-state transport

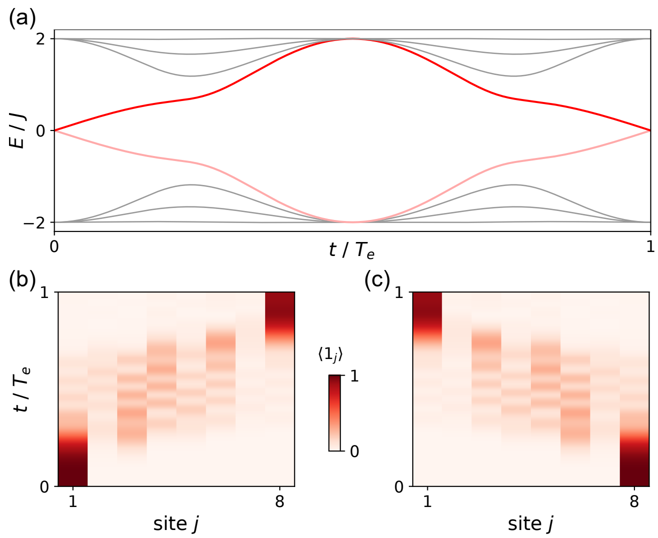

Supplementary Fig. 17. (a) Symmetric energy spectrum of single-particle Rice-Mele model. (b) Transport of a particle from left to right edges. (c) Transport of a particle from right to left edges. The parameters are chosen as $\delta_0/2\pi = J/2\pi = 0.75$ MHz, $\Delta_0/2\pi = 0.5$ MHz, and $T_e = 4$ μs, where Δ_0 and T_e are the same as two-particle edge state pumping in the main texts, and δ_0, J are chosen to be comparable with the effective coupling $J_{\rm eff} \simeq (J+\delta)^2/U$ between $|2_j\rangle$ states [8] in the main texts.

In this subsection, we discuss how the interaction affects edge-state transport. Before taking the interaction into account, we first consider the single-particle case, in which the energy spectrum of the Rice-Mele model is symmetric with respect to zero energy; see Supplementary Fig. 17(a). There are two edge modes in the bulk gap, which provide reversible channels for the transport of edge states from the left end to the right end or vise versa. Because the energies of the two channels are symmetric about zero, the transport from the left to the right edges is symmetric with the reversed process; see Supplementary Fig. 17(b) and (c).

However, when the interaction is involved, the picture becomes different. We consider two initial states in a lattice with 6 sites, one is two particles at the left edge site and the other is two particles at the right edge site. We observe that both the density evolution [Supplementary Fig. 18(a) and (e)] and center-of-mass position shift [Supplementary Fig. 18(b) and (f)] are different in the two cases. This is because the interaction breaks the symmetric energy spectrum in the single-particle case; see Supplementary Fig. 18(c) and (g) and their enlarged views in Supplementary Fig. 18(d) and (h). In the first case, the instantaneous state can follow the eigenstates at the top of the bound-state band, which can be seen as a pumping channel from the left to the right edges (see the red eigenstates in Supplementary Fig. 18(d)). In the latter case, the instantaneous state can follow the eigenstates in the gap between two bound-state bands, which can be viewed as a pumping channel from the right to the left edges (see the red eigenstates in Supplementary Fig. 18(h)). Because both the energy gaps in the two cases are smaller than those in the bulk Thouless pumping, the adiabatic conditions are more stringent than those in the bulk Thouless pumping. Besides, the different energy gaps in the two cases also lead to different adiabatic conditions.

To better understand the physical picture of the asymmetric spectrum in Supplementary Fig. 18(d) and (h), we can approximate the subspace $\mathcal{V}$ consisting of $\{|2_j\rangle\}$ and $\{|1_j\rangle|1_{j+1}\rangle\}$. In the case of $|U| \gg J, \delta, \Delta$, the states of two neighboring particles $\{|1_j\rangle|1_{j+1}\rangle\}$ form intermediate states which can be adiabatically eliminated, and we can obtain an effective Hamiltonian for the bounded particles $\{|2_j\rangle\}$, which turns out to be similar to single-particle Rice-Mele model [8]. However, in the present case where $|U|$ is modest, the subspace of $\{|1_j\rangle|1_{j+1}\rangle\}$ cannot be neglected. In the subspace $\mathcal{V}$, the matrix of the effective Hamiltonian inherits the original interacting Rice-Mele model. To be explicit, the coupling strength between $|2_j\rangle$ and $|1_j\rangle|1_{j+1}\rangle$ is $\sqrt{2}[-J+(-1)^j\delta]$, the onsite energies of $|2_j\rangle$ and $|1_j\rangle|1_{j+1}\rangle$ are $2(-1)^j\Delta+U$, and 0, respectively. By diagonalizing the effective Hamiltonian, we find that the lowest 6 energies are consistent with the spectrum in Supplementary Fig. 18(d) and (h); see Supplementary Fig. 19. Hence, the modest interaction plays a crucial role in the asymmetric spectrum, which cannot be reduced to the simple single-particle Rice-Mele model.

G. Mapping from Thouless pumping to integer quantum Hall effect

For a periodically driven Hamiltonian $H(t) = H(t+T)$, in a Hilbert space formed by Fock states $\{|n_1, n_2, ..., n_N\rangle\}$, the quasieigenstates can be written as

$$|\Psi(t)\rangle = e^{-i\varepsilon_\alpha t} \sum_{m,n_1,\cdots,n_N} e^{im\omega t} C^{\alpha}_{m,n_1,\cdots,n_N} |n_1, \cdots, n_N\rangle, \tag{27}$$

where $C^{\alpha}_{m,n_1,n_2,...,n_N}$ are the amplitudes of the αth eigenstate of the time-independent Floquet operator $\mathcal{H}$, with elements

$$\mathcal{H}_{m,n_1,n_2,...,n_N;m',{}'n'_1,n'_2,...,n'_N} = \frac{1}{T}\int_0^T dt \cdot \langle n_1, ..., n_N| e^{-im\omega t}\left[H(t) - i\partial_t\right] e^{im'\omega t} |n'_1, ..., n'_N\rangle. \tag{28}$$

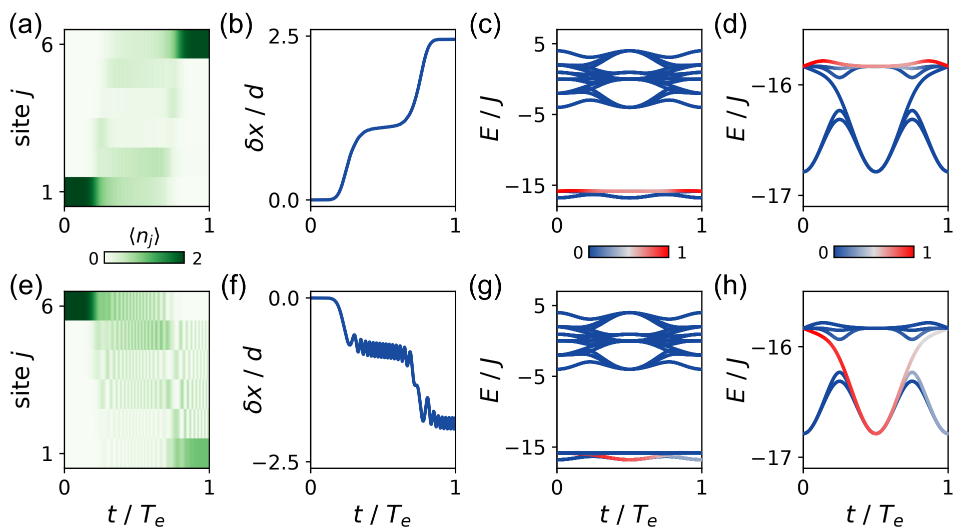

Supplementary Fig. 18. Top panel: the transport of two particles from left to right edges. (a) Density evolution in which the colors denote the density of particles $\langle n_j \rangle$. (b) Mean position shift. (c) Energy spectrum in which the colors denote the probability of the instantaneous state projected into the eigenstates. (d) The enlarged view of (c). Bottom panel: the transport of two particles from right to left edges. (e)-(h) are similar to (a)-(d) but with different initial state. The colors in (a) and (e) denote the density distribution, while the colors in (c),(d),(g),(h) denote the probability of instantaneous states occupying the eigenstates. The parameters are chosen as $J/2\pi = 12$ MHz, $\delta_0/2\pi = 12$ MHz, $\Delta_0/2\pi = 0.5$ MHz, $U/2\pi = -190$ MHz, $T = 4$ μs.

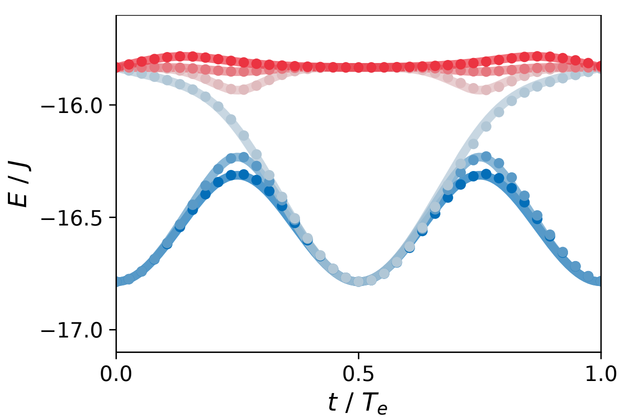

Supplementary Fig. 19. The lowest 6 energies as functions of time. Solid lines are obtained by the original interacting Rice-Mele model and the dots are obtained by the effective Hamiltonian in the subspace of $\mathcal{V}$ consisting of $\{|2_j\rangle\}$ and $\{|1_j\rangle|1_{j+1}\rangle\}$. The parameters are the same as those in Figure 18.

The term of derivative of time contributes to a tilting potential $(m\omega)$ along the Floquet dimension. In the case of a single particle, the states can be alternatively represented by the position of a particle $\{|j\rangle\}$, and the amplitude $C^{\alpha}_{m,j}$ can be obtained by diagonalizing the Floquet Hamiltonian with elements [15],

$$\mathcal{H}_{m,j;m',j'} = \frac{1}{T}\int_0^T \langle j|e^{-im\omega t}[H(t) - i\partial_t]e^{im'\omega t}|j'\rangle dt. \tag{29}$$

Before proceeding to the relation between Thouless pumping and integer quantum Hall effect, we make some remark on the general mapping from one dimension to two dimensions in the single-particle and multi-particle cases based on Eqs. 28 and 29. In the single-particle case, a particle in a one-dimensional periodically driven system can be mapped to a two-dimensional static system with a tilting potential along the Floquet dimension. In the multi-particle case with particle conservation, in a given Floquet index m, the particle number is fixed. When mapping to synthetic two dimensions, all particles as a whole are transferred from the mth to m'th Floquet indices. The tilting energy $m\omega$ is also independent of the particle density. It is totally different from the two-dimensional real-space lattice, where particles could independently hop between different lattices, and the total energy from the tilting potential depends on the particle density.

Taking the Rice-Mele model as an example, in which $\delta(t) = \delta_0 \sin(\omega t + \phi_0)$ and $\Delta(t) = \Delta_0 \cos(\omega t + \phi_0)$ with modulation phase ϕ_0, we will illuminate the one-to-one correspondence between Thouless pumping and the integer quantum Hall effect. In the single particle case, the elements of the Floquet operator are given by

$$\begin{aligned}\mathcal{H}_{m,j,m',j'} &= \delta_{m,m'}\left[m\omega - J(\delta_{j,j'+1}+\delta_{j,j'-1})\right], \\ &+ \delta_{m,m'+1}\left[\frac{\delta_0 e^{i\phi_0}(-1)^j}{2i}\delta_{j,j'-1} + \frac{\delta_0 e^{i\phi_0}(-1)^{j'}}{2i}\delta_{j,j'+1} + \frac{\Delta_0 e^{i\phi_0}(-1)^{j'}}{2}\delta_{j,j'}\right] \\ &+ \delta_{m,m'-1}\left[-\frac{\delta_0 e^{-i\phi_0}(-1)^j}{2i}\delta_{j,j'-1} - \frac{\delta_0 e^{-i\phi_0}(-1)^{j'}}{2i}\delta_{j,j'+1} + \frac{\Delta_0 e^{-i\phi_0}(-1)^{j'}}{2}\delta_{j,j'}\right],\end{aligned} \tag{30}$$

where $\delta_{m,m'}$ is the Kronecker delta function. To better understand the above equation, we show the connection of the synthetic two-dimensional lattice; see Supplementary Fig. 20. We can find that there is tilting potential along the synthetic lattice direction and three kinds of hopping processes: nearest-neighboring hopping along the real lattice direction, nearest-neighboring hopping along the synthetic lattice direction due to time modulation of onsite energy, and next-nearest neighboring hopping due to time modulation of hopping strength. We first neglect the tilting potential and find that the two-dimensional synthetic lattice has translational symmetry. There are two lattice sites in a unit cell, indicating that there are two energy bands in the momentum space. The energy bands can be obtained by applying the Bloch theorem, with which the Bloch functions are given by

$$\begin{aligned}\psi_{k_x,k_y}(2j-1,m) &= Ae^{-ik_y m}e^{-ik_x(2j-1)}, \\ \psi_{k_x,k_y}(2j,m) &= Be^{-ik_y m}e^{-ik_x 2j},\end{aligned} \tag{31}$$

where $k_{x(y)}$ is the quasimomentum in the $x(y)$ direction. By solving the Schrödinger equation $\mathcal{H}\psi_{k_x,k_y} = E\psi_{k_x,k_y}$, we can find that the coefficients (A, B) can be obtained by diagonalizing the following Hamiltonian,

$$H_{k_x,k_y} = \begin{bmatrix} -\Delta_0\cos(k_y+\phi_0) & 2[J\cos(k_x)+i\delta_0\sin(k_y+\phi_0)\sin(k_x)] \\ 2[J\cos(k_x)-i\delta_0\sin(k_y+\phi_0)\sin(k_x)] & \Delta_0\cos(k_y+\phi_0)\end{bmatrix} \tag{32}$$

This equation is equivalent to the Hamiltonian in the (k, t) space [16], if we replace k_y with ωt. It means that the phases between the two-dimensional synthetic lattice and the one-dimensional periodically modulated lattice are the same. Now, we can discuss the relation between Thouless pumping and integer quantum Hall effect. In both cases, we prepare an initial Wannier state which uniformly occupies the Bloch state in a given band along the k_x direction. In the one-dimensional periodically modulated lattice, the mean position shift in a pumping cycle is equal to a unit cell. While in the two-dimensional synthetic lattice, due to the tilting potential, the particle will undergo a Bloch oscillation along the synthetic direction, and the mean position shift along the real-space direction in a period of Bloch oscillation is also equal to a unit cell. The mean position shift along the real-space direction is the same in both cases. That is why the Thouless pumping can be viewed as a dynamical version of integer quantum Hall effect.

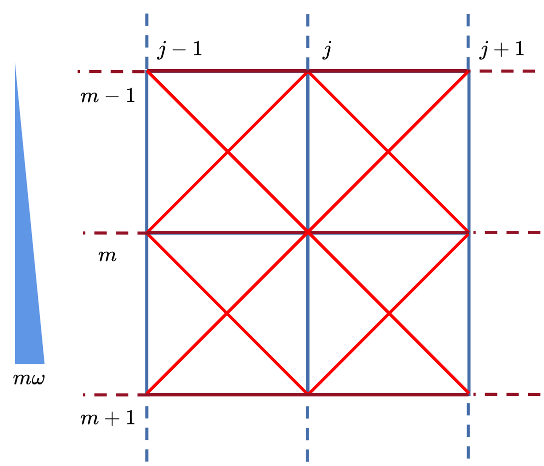

Supplementary Fig. 20. The mapping of Rice-Mele model to a two-dimensional synthetic lattice for integer quantum Hall effect. Apart from Harper-type model, There is an additional tilting potential along the synthetic direction.

In the multi-particle cases, the mapping from Thouless pumping to two-dimensional integer quantum Hall effect is somehow tricky. We cannot simply add interacting particles in the two-dimensional synthetic lattice subjected to tilting potential along the synthetic direction. This is because we need to consider the restriction that the particle number is conserved for a given Floquet index m. It means that all the particles jump between subspaces with different Floquet indices as a whole. The particles independently tunnel along the real-space direction but behave as bounded particles along the synthetic direction. This is in stark contrast to the case of interacting particles in a real two-dimensional lattice.

H. Numerical simulation of qutrit dynamics

We give the numerical simulation of qutrit dynamics using the Lindblad master equation with the QuTiP python library [17]. The full Hamiltonian is given as

$$H/\hbar = \sum_{j=1}^{N-1}\left[[-J+(-1)^j\delta]a_j^\dagger a_{j+1} + \text{H.c.}\right] + \sum_{j=1}^{N}\left[(-1)^j\Delta a_j^\dagger a_j + \frac{U}{2}a_j^\dagger a_j^\dagger a_j a_j\right], \tag{33}$$

where

$$\begin{aligned} a_j &= I\otimes I\otimes\cdots a\otimes I\cdots, \\ a_j^\dagger &= I\otimes I\otimes\cdots a^\dagger\otimes I\cdots, \end{aligned} \tag{34}$$

and $\otimes$ is tensor product. The lowest three energy levels $|n\rangle$ $(n=0,1,2)$ of our superconducting qutrits are considered, $|0\rangle=(1,0,0)^T$, $|1\rangle=(0,1,0)^T$, $|2\rangle=(0,0,1)^T$, which give the annihilation and creation operators in a matrix form

$$a = \begin{pmatrix}0 & 1 & 0\\ 0 & 0 & \sqrt{2}\\ 0 & 0 & 0\end{pmatrix}, \quad a^\dagger = \begin{pmatrix}0 & 0 & 0\\ 1 & 0 & 0\\ 0 & \sqrt{2} & 0\end{pmatrix}. \tag{35}$$

As the decoherence parameters depend on the qutrit frequencies, it is difficult to accurately model pumping dynamics with time-varying decoherence. For simplicity, the numerical calculation results in the main text are obtained without decoherence.

We give the numerical results as supplementary analysis for Thouless pumping of two bounded microwave photons when considering decoherence effects in the qutrits, as shown in Supplementary Fig. 21. The numerical results as supplementary analysis for resonant tunneling of interacting photons when considering decoherence effects in the qutrits is shown in Supplementary Fig. 22.

Supplementary Fig. 23 gives the numerical results of edge state pumping when considering decoherence effects in qutrits. We note that the fast oscillation features on populations are hardly captured by the present experiment, which is mainly due to the possible readout errors and fluctuations on the experimental controlled parameters including qubit and coupler frequencies during the pumping process.

Supplementary Fig. 24 gives the numerical results of Thouless pumping of two-particle edge states with the period $T_e = 40$ μs without considering decoherence effects, where the non-adiabatic effects of pumping from the right edge state are suppressed and the dynamics become similar to the reversal pumping from the left edge state, as compared to the case of short $T_e = 4$ μs in Fig. 4 in the main text.

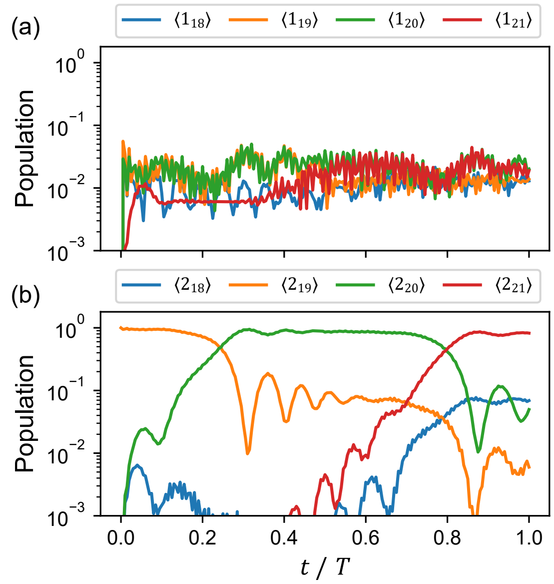

Supplementary Fig. 21. Numerical simulation for Thouless pumping of two bounded microwave photons when considering decoherence effects, showing the population of (a) $|1_j\rangle$ and (b) $|2_j\rangle$. Here, we consider the same parameters used in Fig. 2 of the main text: $\Delta_0/2\pi = 8$ MHz, $\delta_0/2\pi = J/2\pi = 12$ MHz and a pumping period of $T = 0.4$ μs.

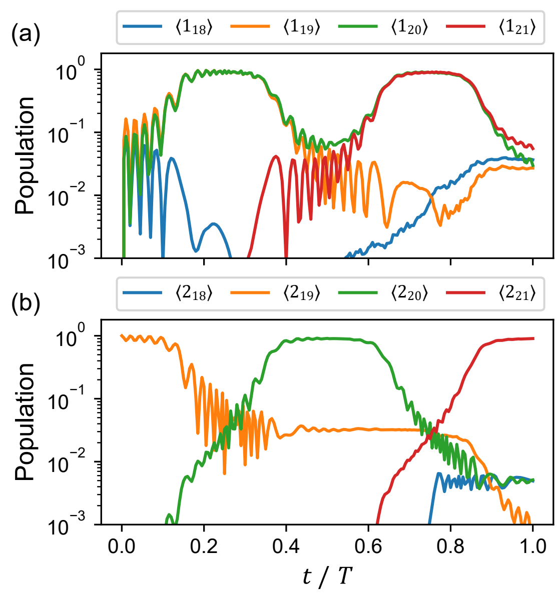

Supplementary Fig. 22. Numerical simulation for resonant tunneling for interacting photons when considering decoherence effects, showing the population of (a) $|1_j\rangle$ and (b) $|2_j\rangle$. Here, we consider the same parameters used in Fig. 3 of the main text: $\Delta_0/2\pi = 150$ MHz, $\delta_0/2\pi = J/2\pi = 12$ MHz and a pumping period of $T = 0.4$ μs.

VI. Robustness of pumping process

We further explore the robustness of single-particle Thouless pumping to different sources of imperfection, including the pumping period, on-site interaction disorder, on-site energy offset and disorder.

A. Adiabaticity versus decoherence

Supplementary Fig. 25 shows single-particle Thouless pumping with different pumping period T, where the non-adiabatic effects for a short T and decoherence for a long T contribute to the deviations from ideal pumping, respectively. Since the energy relaxation and pure dephasing times during the qutrit and coupler frequency modulation are dynamical and much shorter than the case at the idle point [5], we consider a static effective energy relaxation and pure dephasing time in the numerical simulation of master equation which fits the experimental results well with long pumping periods.

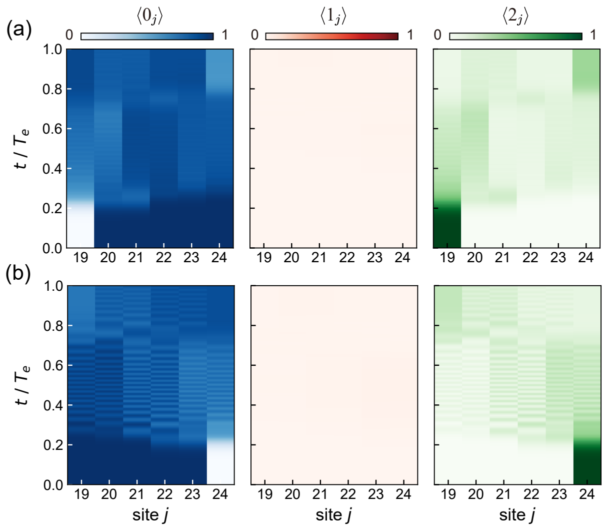

Supplementary Fig. 23. Numerical simulation of the left (a) and right (b) edge state pumping when considering decoherence effects in qutrits, where $\Delta_0/2\pi = 0.5$ MHz, $\delta_0/2\pi = J/2\pi = 12$ MHz and $T_e = 4$ μs.

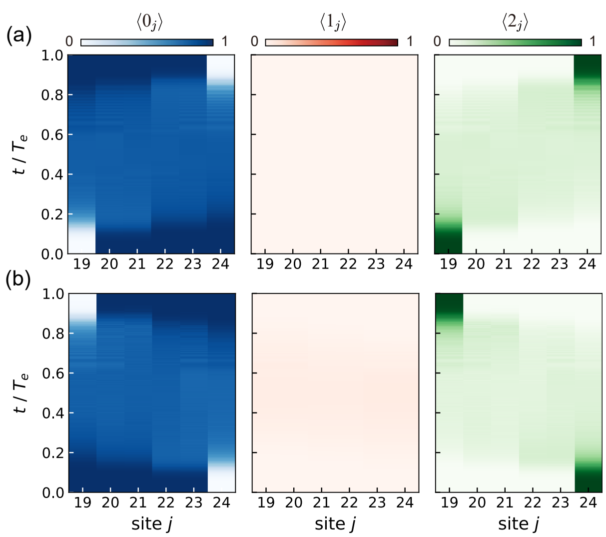

Supplementary Fig. 24. Numerical simulation of the left (a) and right (b) edge state pumping for $T_e = 40$ μs, where $\Delta_0/2\pi = 0.5$ MHz, $\delta_0/2\pi = J/2\pi = 25$ MHz.

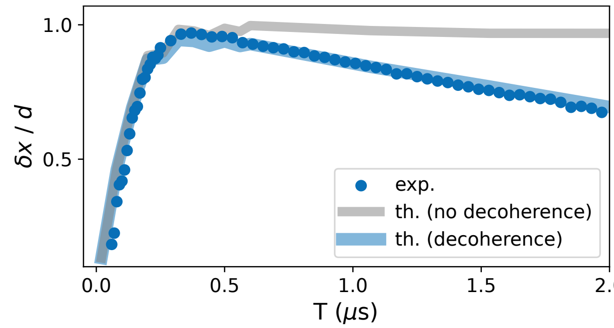

Supplementary Fig. 25. Center of mass displacement $\delta x = d/2 \sum j n_j / \sum n_j$ for single-particle pumping with different pumping period T. The blue dots are experimental data, the blue and grey curves are numerical simulations with and without decoherence, respectively. The effective energy relaxation time $T_1^{\text{eff}} = 25$ μs and pure dephasing time $T_\phi^{\text{eff}} = 1$ μs are considered for the blue curve, which are contributed from the qutrit dephasing away from the sweet spot and the coupling between the qutrit and the less coherent coupler [5].

B. On-site interaction disorder

In this experiment, the strength of the on-site interaction varies for different sites due to the imperfection of the sample, as shown in Supplementary Fig. 26.

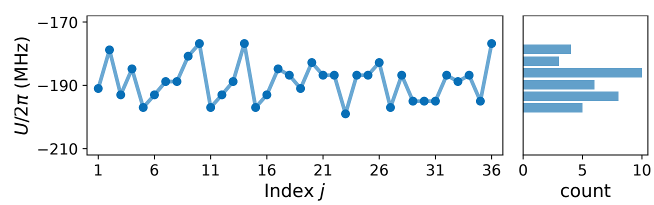

Supplementary Fig. 26. The strength of on-site interaction for each site by measuring the anharmonicity of qutrits.

It is of importance to study the effect of disordered interaction on the Thouless pumping of bounded particles. In 1D systems, the eigenstates become localized in the presence of disordered tunneling strength or on-site potential according to the Anderson's theory [18]. Similarly, the disordered on-site interaction strength will lead to a localization effect on the bounded particles.

We show the energy spectrum during the pumping process by considering the disordered on-site interaction in Figure 27. Notably, the bands in Supplementary

Fig. 27(a) are mixed near $t = T/4$ and $t = 3T/4$, and the band corresponding to the resonant tunneling in Supplementary Fig. 27(b) stays gapped during the whole pumping process. It seems that the pumping of bounded particles will be broken in Supplementary Fig. 27(a), since the energy gap vanishes and therefore the adiabatic condition is broken. However, due to the disordered interaction, eigenstates are localized at different sites, and they are not coupled unless the two wavefunctions are overlapped. To demonstrate this effect, we calculate the average position of the eigenstate and mark them in the energy spectrum, as shown in Supplementary Fig. 28. It can be seen that the eigenstates located at different sites are independent during the pumping process because they do not overlap. Meanwhile, the overlapped eigenstates present avoid crossing with an energy gap $\Delta E \approx 0.5J$. This fact means that the adiabatic condition can still be satisfied and that the pumping is immune to the disordered interaction in this experiment. The numerical analysis here is in accordance with the experimental result in the main text, where the pumping is robust. On the other hand, we remark that slightly disordered interaction will suppress the spread of the wave packet during the pumping, which is beneficial.

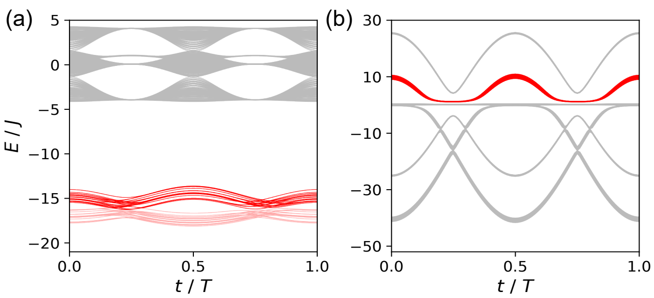

Supplementary Fig. 27. Energy spectrum in the presence of disordered interaction. (a) and (b) show the energy spectrum during the pumping of bounded particles and resonant tunneling respectively. The bands of bounded particles we focus on are marked by red and pink colors. The parameters are the same as Supplementary Fig. 15 and Supplementary Fig. 16 except for the disordered interaction strength given in Supplementary Fig. 26.

C. On-site energy offset

In Supplementary Fig. 29, we add a relative on-site energy offset Δ_r to Δ, i.e., $\Delta = \Delta_0[\sin(\omega t) + \Delta_r]$, and measure the Loschmidt echo $\mathcal{L} = |\langle\psi(t)|\psi(t=0)\rangle|^2$ which is the recovery of evolving quantum states [19, 20],where the initial state $\psi(t=0) = |1_{j=18}\rangle$. When the relative offset $\Delta_r < 1$, the degeneracy point remains encircled by the trajectory $\mathcal{C}$ in the $\Delta - \delta$ parameter plane, and the pump cycles are hardly affected by the offset, as indicated by $\mathcal{L} \approx 0$. When $\Delta_r > 1$, $\mathcal{C}$ no longer encircles the degeneracy point, as a consequence, the pumping cycles are dramatically changed, as indicated by the step change in $\mathcal{L}$.

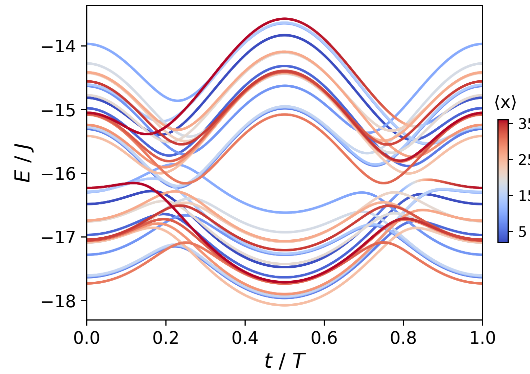

Supplementary Fig. 28. Enlarged area of the energy spectrum. We mark each eigenenergy by the average position $\langle x\rangle = \langle\psi|\hat{x}|\psi\rangle$. The parameters are the same as Supplementary Fig. 15.

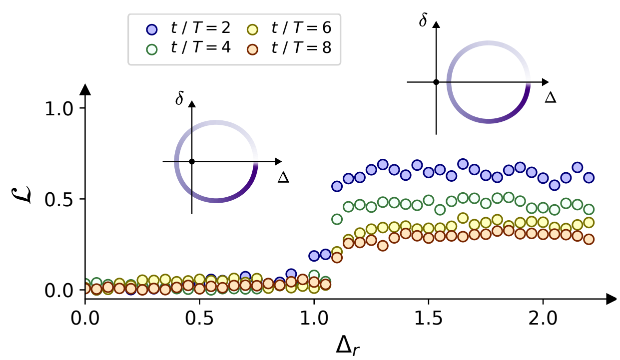

Supplementary Fig. 29. Measured Loschmidt echo $\mathcal{L}$ against Δ_r under $t/T = 2, 4, 6, 8$.

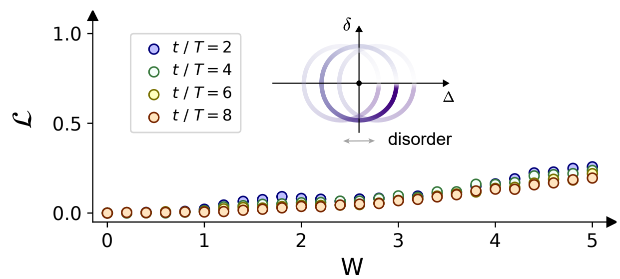

Supplementary Fig. 30. Measured Loschmidt echo $\mathcal{L}$ against W under $t/T = 2, 4, 6, 8$, where each point is averaged over 50 times with random disorder to Δ.

D. On-site energy disorder

In Supplementary Fig. 30, we add several random disorder to Δ, with $\Delta = \Delta_0[\sin(\omega t) + W\xi_l]$, where

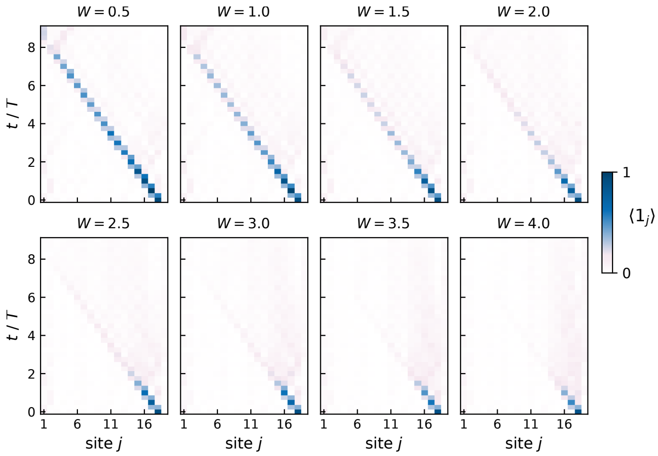

Supplementary Fig. 31. The population of $|n\rangle_j$ during the disordered pumping process with W =0.5, 1.0, 1.5, $\cdots$, 4.0.

$\xi_l \in [-0.5, 0.5]$ is a uniformly distributed random number, and W is the disorder weight relative to Δ_0. The evolution of particle populations $|1_j\rangle$ under the on-site energy disorder is given in Supplementary Fig. 31, which shows transition from localized to delocalized population with increasing W.

[1] J. Koch, T. M. Yu, J. Gambetta, A. A. Houck, D. I. Schuster, J. Majer, A. Blais, M. H. Devoret, S. M. Girvin, and R. J. Schoelkopf, Phys. Rev. A **76**, 042319 (2007).

[2] A. Blais, A. L. Grimsmo, S. M. Girvin, and A. Wallraff, Rev. Mod. Phys. **93**, 025005 (2021).

[3] P. Krantz, M. Kjaergaard, F. Yan, T. P. Orlando, S. Gustavsson, and W. D. Oliver, Appl. Phys. Rev. **6**, 021318 (2019).

[4] R. Barends, J. Kelly, A. Megrant, D. Sank, E. Jeffrey, Y. Chen, Y. Yin, B. Chiaro, J. Mutus, C. Neill, *et al.*, Phys. Rev. Lett. **111**, 080502 (2013).

[5] Y. Xu, J. Chu, J. Yuan, J. Qiu, Y. Zhou, L. Zhang, X. Tan, Y. Yu, S. Liu, J. Li, *et al.*, Phys. Rev. Lett. **125**, 240503 (2020).

[6] B. Saxberg, A. Vrajitoarea, G. Roberts, M. G. Panetta, J. Simon, and D. I. Schuster, Nature (London) **615**, 435 (2022).

[7] A. F. Linskens, I. Holleman, N. Dam, and J. Reuss, Phys. Rev. A **54**, 4854 (1996).

[8] Y. Ke, X. Qin, Y. S. Kivshar, and C. Lee, Phys. Rev. A **95**, 063630 (2017).

[9] M. C. Collodo, J. Herrmann, N. Lacroix, C. K. Andersen, A. Remm, S. Lazar, J.-C. Besse, T. Walter, A. Wallraff, and C. Eichler, Phys. Rev. Lett. **125**, 240502 (2020).

[10] J. Niu, L. Zhang, Y. Liu, J. Qiu, W. Huang, J. Huang, H. Jia, J. Liu, Z. Tao, W. Wei, *et al.*, Nat. Electron. **6**, 235 (2023).

[11] A. Dunsworth, A. Megrant, C. Quintana, Z. Chen, R. Barends, B. Burkett, B. Foxen, Y. Chen, B. Chiaro, A. Fowler, *et al.*, Appl. Phys. Lett. **111**, 022601 (2017).

[12] A. Dunsworth, R. Barends, Y. Chen, Z. Chen, B. Chiaro, A. Fowler, B. Foxen, E. Jeffrey, J. Kelly, P. V. Klimov, *et al.*, Appl. Phys. Lett. **112**, 063502 (2018).

[13] Y. Zhou, Z. Zhang, Z. Yin, S. Huai, X. Gu, X. Xu, J. Allcock, F. Liu, G. Xi, Q. Yu, *et al.*, Nat. Commun. **12**, 5924 (2021).

[14] E. Jeffrey, D. Sank, J. Mutus, T. White, J. Kelly, R. Barends, Y. Chen, Z. Chen, B. Chiaro, A. Dunsworth, *et al.*, Phys. Rev. Lett. **112**, 190504 (2014).

[15] A. Gómez-León and G. Platero, Phys. Rev. Lett. **110**, 200403 (2013).

[16] Y. Ke, S. Hu, B. Zhu, J. Gong, Y. Kivshar, and C. Lee, Phys. Rev. Research **2**, 033143 (2020).

[17] J. Johansson, P. Nation, and F. Nori, Comput. Phys. Commun. **183**, 1760 (2012).

[18] P. W. Anderson, Phys. Rev. **109**, 1492 (1958).

[19] K. Xu, Z.-H. Sun, W. Liu, Y.-R. Zhang, H. Li, H. Dong, W. Ren, P. Zhang, F. Nori, D. Zheng, *et al.*, Sci. Adv. **6**, eaba4935 (2020).

[20] S. K. Zhao, Z.-Y. Ge, Z. Xiang, G. M. Xue, H. S. Yan, Z. T. Wang, Z. Wang, H. K. Xu, F. F. Su, Z. H. Yang, *et al.*, Phys. Rev. Lett. **129**, 160602 (2022).